Anomalous anticrossing of neutral exciton states in GaAs/AlGaAs quantum dots

S. Kumar,[1,3,*] E. Zallo,[1] Y. H. Liao,[2] P. Y. Lin,[2] R. Trotta,[1,4] P. Atkinson,[1,5] J. D. Plumhof,[1] F. Ding,[1] B. D. Gerardot,[3] S. J. Cheng,[2] A. Rastelli,[1,4] and O. G. Schmidt[1,6,7]

[1] *Institute for Integrative Nanosciences, IFW Dresden, Helmholtzstraße 20, 01069 Dresden, Germany*
[2] *Department of Electrophysics, National Chiao Tung University, Hsinchu 300, Taiwan, Republic of China*
[3] *Institute of Photonics and Quantum Sciences, SUPA, Heriot-Watt University, Edinburgh EH14 4AS, UK*
[4] *Institute of Semiconductor and Solid State Physics, Johannes Kepler University Linz, Altenbergerstraße 69, 4040 Linz, Austria*
[5] *Institut des Nanosciences de Paris, UPMC-CNRS UMR 7588, 4 Place Jussieu Boite Courrier 840, 75252 Cedex 05, France*
[6] *Technische Universität Chemnitz, Material Systems for Nanoelectronics, Reichenhainer Straße 70, 09107 Chemnitz, Germany*
[7] *Center for Advancing Electronics Dresden, Technische Universität Dresden, 01067 Dresden, Germany*

(Received 24 November 2013; revised manuscript received 13 February 2014; published 12 March 2014)

We study the effects of heavy hole–light hole (HH-LH) mixing on fine-structure and polarization properties of neutral excitons (X^0) confined in single GaAs/AlGaAs quantum dots (QDs) under the application of anisotropic biaxial stress. In the large HH-LH mixing regime, these properties are substantially different from the usually observed properties in the case of small or no mixing. By varying the applied stress, the mixing in the initially *strain-free* QDs changes from ∼0 to ∼70% and an anomalous anticrossing of the X^0 bright states is observed. The latter is attributed to stress-induced rotation of the in-plane principal axis of the QD confinement potential. We show that the analysis of free-excitonic emission of bulk GaAs surrounding the QDs not only allows estimation of the stress and mixing in the QDs, but also provides the quantum-confinement-induced HH-LH splitting of the as-grown QDs.

DOI: 10.1103/PhysRevB.89.115309 PACS number(s): 73.21.La, 71.35.−y, 73.20.Mf, 81.07.Ta

I. INTRODUCTION

The reduced symmetry of most as-grown quantum dots (QDs) leads to mixing of the two neutral bright excitonic states due to the electron-hole spin-exchange interaction, and therefore the emission splits into two lines which are usually linearly polarized along orthogonal directions. The energetic separation between these lines is called fine-structure splitting (FSS) [1,2] and the reduction of it to zero, either by growth optimization [3–5] or by external perturbations such as magnetic field [6], electric field [7], strain [8], or combined electric and strain fields [9] is required for the generation of polarization-entangled photon pairs via the biexcitonic-excitonic cascade [6,7]. The mixing of heavy-hole (HH) bright excitonic states with the light-hole (LH) bright excitonic states introduces a polarization anisotropy (i.e., unequal emission intensities) between these two FS-split lines [10,11]. Sufficiently large HH-LH mixing results in nonorthogonal linearly polarized X^0 lines [12,13]. Finite HH-LH mixing is expected to have an impact on hole-spin relaxation [14] and decoherence [15] in QDs, but this aspect has yet to be investigated experimentally. As single-particle (electron or hole) spins and entangled photon pairs have been suggested for constructing stationary and flying qubits, respectively, for quantum networks with nodes [16], understanding of HH-LH mixing and its effect on the optical properties of quasiparticles confined in QDs is crucial. An anisotropic confinement potential [17] and the presence of anisotropic intrinsic strain [12,13] as well as composition fluctuations [17] in conventional Stranski-Krastanow QDs all contribute to their optical properties, making it a complicated system to understand the origin of HH-LH mixing. *Strain-free* GaAs/AlGaAs QDs [18,19], for which composition fluctuations are strongly reduced and which can be grown in highly symmetric shapes [20], represent a simpler system to investigate the effects of external perturbations.

In this work, we investigate experimentally and theoretically the fine-structure and polarization properties of the X^0 emission of single GaAs/AlGaAs QDs in the regime of large anisotropic biaxial stress. We find that the variations of FSS and polarization directions of both X^0 lines as a function of stress show an anomalous anticrossing behavior due to rotation of the in-plane principal axis of the QD confinement potential (i.e., symmetry axis). We demonstrate that HH-LH mixing parameters extracted using two different approaches are in a fairly good agreement with each other. The first and conventional approach is to use the total emission intensity of both X^0 lines, whereas the second is based on the experimental estimation of the stresses inside the QDs via the change in the free-excitonic emission of the stressed bulk GaAs surrounding the QDs. This approach also allows us to estimate the quantum-confinement-induced HH-LH splitting of the as-grown QDs.

II. SAMPLES AND METHODS

The GaAs/AlGaAs QD sample was grown by molecular beam epitaxy following the procedure reported by Atkinson *et al.* [21]: first nanoholes are created on a GaAs surface using in situ Ga-droplet etching; the holes are then overgrown with 7 nm $Al_{0.44}Ga_{0.56}As$ and filled by 3 nm GaAs followed by a 2 min growth interruption. The resulting GaAs dots have an irregular shape with a height of about 8 nm and widths of about 45/65 nm in the $[1\bar{1}0]/[110]$ directions. See Fig. 1(a) of Ref. [22] for representative line scans. A 260-nm-thick membrane containing QDs was grown on top of a 100-nm-thick $Al_{0.75}Ga_{0.25}As$ sacrificial layer on a semi-insulating GaAs (100) substrate. Besides the QDs,

*Santosh.Kumar@hw.ac.uk

 ©2014 American Physical Society

the membrane includes a 99-nm-thick GaAs layer (see Ref. [19] for the sample structure), which we use here as a local strain-gauge, as explained later. The detachment of the membrane from the substrate was accomplished by patterning the sample into rectangular mesas (100×120) μm^2 by optical lithography and wet-etching using H_2SO_4:H_2O_2:H_2O down to the sacrificial layer. This layer was then removed by diluted HF. The underetched membranes lying on the substrate were finally transferred upside down onto the surface of a 300-μm-thick $[Pb(Mg_{1/3}Nb_{2/3})O_3]_{0.72}$-$[PbTiO_3]_{0.28}$ (PMN-PT) actuator using gold-thermocompression bonding [23]. The bonding process induces in-plane stress in the membranes, which can be varied by applying an out-of-plane electric field (F_p) to the PMN-PT substrate. The positive (negative) F_p corresponds to application of an additional in-plane compressive (tensile) stress in the membranes.

Polarization-resolved micro-photoluminescence (μ-PL) measurements under nonresonant excitation were performed at $T = 8$ K using a 0.75 m focal length spectrometer and liquid-nitrogen-cooled silicon CCD detector. Higher resolution measurements were performed using a double spectrometer with 0.75 m focal length per stage. The spectral resolution of the single (double) spectrometer at a wavelength of 780 nm is $\sim$40 μeV ($\sim$20 μeV). The polarization of the PL signal was analyzed by combining a rotatable achromatic half-wave plate and a fixed linear polarizer.

To measure the polarization direction of the PL signal with respect to the GaAs crystal directions, an as-grown QD sample was taken as a reference. During the optical lithography process rectangular membranes were fabricated, where the longer side was parallel to the [110] crystal direction. We mounted a cleaved piece of an as-grown sample as well as the sample with membranes in such a way that the [110] ($[1\bar{1}0]$) crystal axis of the membranes aligns with the [110] ($[1\bar{1}0]$) crystal axis of the as-grown sample, as shown schematically in Fig. 1(a). The statistical measurement of the polarization directions of the neutral excitonic X^0 emission of *strain-free* GaAs QDs from the as-grown sample was used to calibrate the [110] or $[1\bar{1}0]$ crystal directions as explained in the following. Figure 1(b) shows a μ-PL polarization map of the emission of a single QD from the as-grown sample showing emission intensity as function of the emission energy and the polarization angle with respect to the axis of the linear polarizer. The wavelike pattern is attributed to FS-split linearly polarized X^0 emission of the QD. The solid line is the cosine fit of the fitted peak energies, which were obtained by fitting the measured peak at each polarization angle by a Lorentzian function. The peak-to-peak energetic distance of the cosine fit was assigned as the FSS of the X^0 emission and the angular positions corresponding to low-energy and high-energy extremum were assigned as linear polarization directions of the low-energy (dotted line) and high-energy X^0 lines.

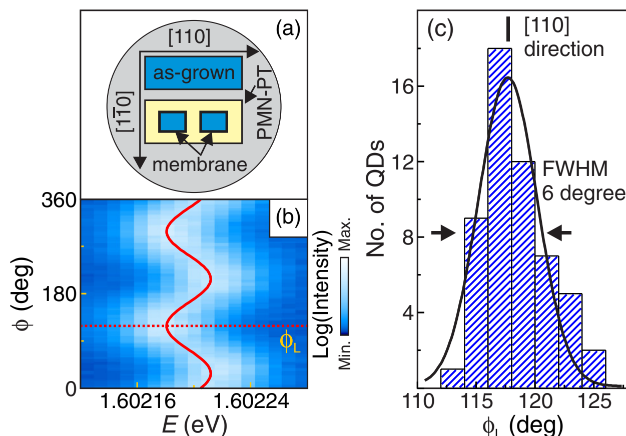

FIG. 1. (Color online) (a) Schematic representation of the samples onto the cold finger. (b) μ-PL polarization maps of the X^0 emission of a single QD from the as-grown sample. ϕ is the polarization rotation angle introduced by the half-wave plate with respect to the axis of the linear polarizer and ϕ_L is the polarization direction of the low-energy component of the X^0 emission. (c) Histograms of ϕ_L of 54 as-grown QDs.

Figure 1(c) shows a histogram of the polarization directions of the low-energy X^0 line of 54 measured QDs from the as-grown sample. A very narrow distribution (solid line) with a full width at half maximum of 6° centered at 118° can be seen, which indicates that the polarization directions of most of the QDs are aligned along certain crystal directions. Theory [10] and measurements [21] confirm that this direction is the [110] crystal direction (see Fig. 1(b) of Ref. [20]) because the GaAs QDs are elongated in this direction. Therefore, we assigned 118° as the angular position of the [110] crystal direction. In the following all angles will be measured with respect to this direction.

III. RESULTS AND DISCUSSION

Figures 2(a) and 2(b) show polarization-resolved color-coded PL intensity maps for QD-A from the as-grown sample and for QD-B from the membrane at $F_p = 0$, respectively. The intensities of the emission are plotted as a function of the emission energy and the polarization angle (ϕ, measured positive counterclockwise with respect to the [110] direction). We resolve two FS-split lines of the X^0 emission for QD-A and QD-B, which are linearly polarized. The values of FSS for QD-A and QD-B are 33 and 150 μeV, respectively. The corresponding intensities of each X^0 line, obtained by fitting with Lorentzian functions, are shown in Figs. 2(e) and 2(f) together with cosine fits (solid lines). The angular positions of the maxima, ϕ_L and ϕ_H, i.e., the polarization directions of the low- and high-energy X^0 lines, respectively, are shown by dotted lines.

As shown in Fig. 2(e), QD-A shows orthogonal X^0 states and ϕ_L and ϕ_H are nearly aligned along the [110] and $[1\bar{1}0]$ directions. Slight misalignments of these states can be ascribed to the misalignment of the QD symmetry axis [13,24] with respect to the [110] crystal direction [see statistical distribution of ϕ_L in Fig. 1(c)].

Contrarily, the X^0 states of QD-B at $F_p = 0$ [see Fig. 2(f)] are not aligned with the crystallographic directions and their angular separation, $\Delta\phi = |\phi_L - \phi_H| = 53°$, strongly deviates from the common orthogonal configuration. The statistical distributions of $\Delta\phi$ for QDs from the as-grown sample and for QDs from a single membrane at $F_p = 0$ [see Figs. 3(a) and 3(b)] were found within 88°–94° and 30°–85°, respectively.

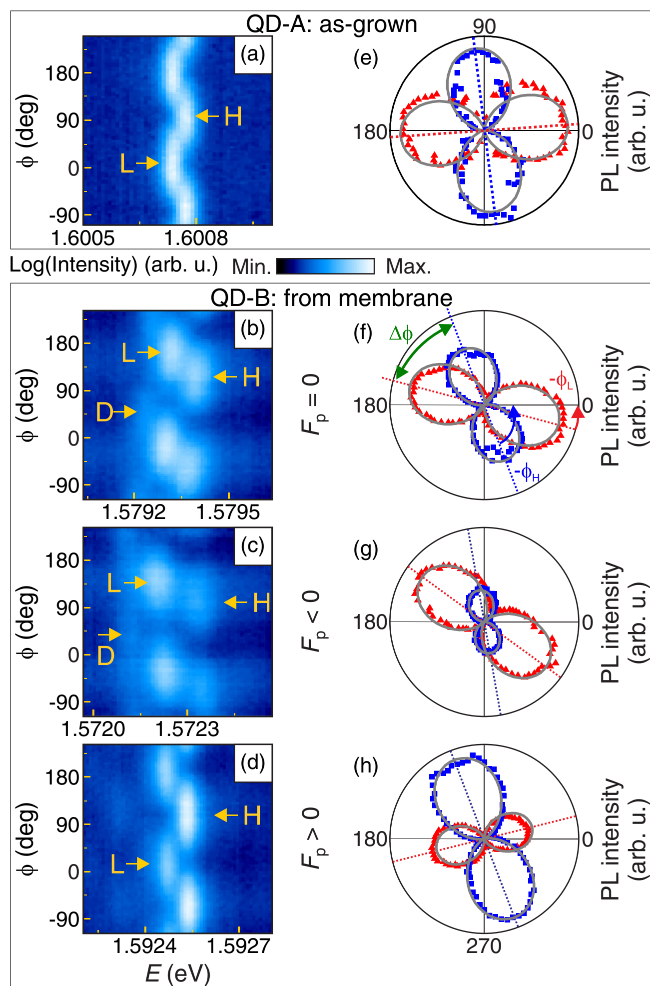

FIG. 2. (Color online) μ-PL polarization maps of the X^0 emission for (a) QD-A and for QD-B (b) at no applied stress ($F_p = 0$ kV/cm), (c) under applied tensile stress ($F_p = -6.7$ kV/cm), and (d) under applied compressive stress ($F_p = 26.7$ kV/cm). Labels L (H) and D refer to low- (high-) energy bright X^0 line and dark X^0 line, respectively. (e), (f), (g), and (h) Polar plots of the intensities of the low-energy (triangles) and high-energy (squares) X^0 lines shown in (a), (b), (c), and (d), respectively. The gray lines are the fits.

Additionally, a substantial anisotropy in the emission intensities of the two X^0 lines can be seen in Fig. 2(f). The observation of large FSS, non-orthogonality and intensity anisotropy of the X^0 emission for QD-B and other QDs from the membrane can be partially ascribed to anisotropic static stress in the membrane, which is attributed to thermal-stress generated by thermal expansion/contraction coefficients mismatch of materials during sample cool-down. Section III C describes this in detail. Figure 2(b) shows also a weak emission line D on the lowest energy side, which is also linearly polarized [see spectra in Fig. 3(c) corresponding to the polarization directions of all three lines]. This line is tentatively assigned to the emission associated with the dark X^0 states, which can become optically active due to stress-induced symmetry breaking of the crystal [25,26]. We have extracted the values of the energetic splitting of line D from the center of the X^0 doublet (i.e., dark-bright splitting) and they are in a range of 90 to 130 μeV.

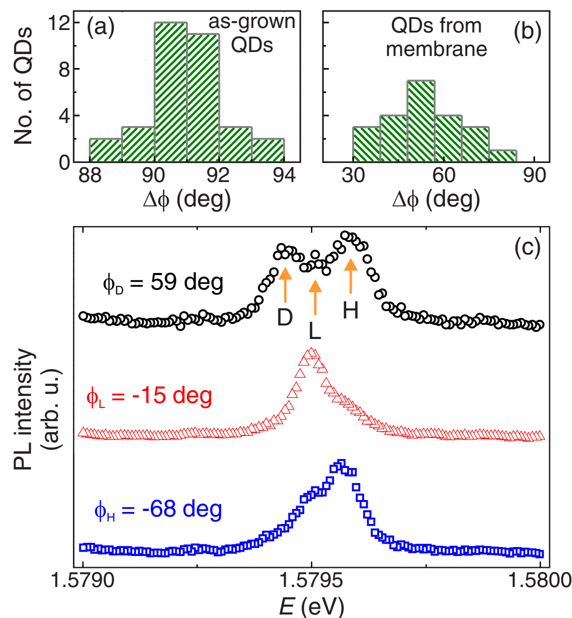

FIG. 3. (Color online) Histograms of $\Delta\phi$ for QDs (a) from the as-grown sample and (b) from a single membrane, respectively. (c) μ-PL spectra of X^0 emission of QD-B at $F_p = 0$ kV/cm along the polarization directions of the lowest- (circles), low- (triangles), and high- (squares) energy lines. The peaks positions of all three lines are shown by arrows.

Our measured values fall within the range of previous reports for the dark-bright splitting of $In_{0.60}Ga_{0.40}As$ QDs [27] and GaAs "natural dots" in quantum wells [28]. Notably, the D line is observed here without the application of any external magnetic field, which is often used to reveal the dark exciton [29]. In the following we discuss the effect of variable stresses on the emission properties of our QDs and of the GaAs layer located above them.

A. Stress-dependent FSS and polarization properties of QDs

The application of additional stress changes the X^0 emission properties substantially as illustrated in Figs. 2(c) and 2(g) for tensile stress (at $F_p = -6.7$ kV/cm) and in Figs. 2(d) and 2(h) for compressive stress (at $F_p = 26.7$ kV/cm). In the investigated range of F_p, the emission energy varies by more than 20 meV. Figure 4 summarizes the F_p-dependent FSSs and polarization properties of QD-B and QD-C (another QD selected from the same membrane as QD-B). Figures 4(a)–4(d) show FSSs, ϕ_L (triangles) and ϕ_H (squares), polarization anisotropy [defined as I_H/I_L, where $I_{L(H)}$ is the maximum intensity of the low- (high-) energy X^0 line], and normalized maximum total intensity of both lines as a function of F_p for QD-B. Similar plots for QD-C are shown in Figs. 4(e)–4(h). The FSSs of both QDs first decrease with increase in F_p, reach minimum values, and then increase with increase in F_p. Such a behavior resembles the anticrossing of bright X^0 states, which has been reported previously [7–9]. However, the FSS minimum values, reached at a field F_p^* for both QDs, are relatively large (57 and 51 μeV for QD-B and QD-C, respectively). As discussed below, we attribute this observation to the fact that the directions of the principal

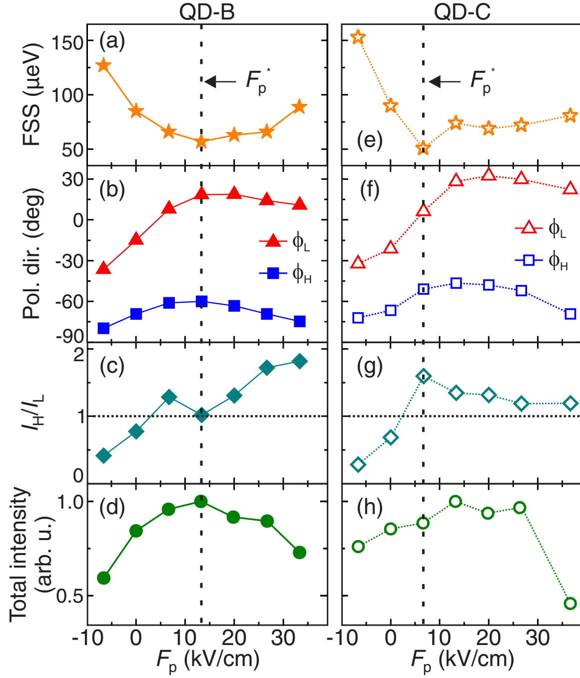

FIG. 4. (Color online) Left: Plots of (a) FSS, (b) ϕ_L (triangles) and ϕ_H (squares), (c) I_H/I_L, and (d) I_T versus F_p for QD-B. Right: (e)–(h) Similar plots for QD-C. All closed (open) symbols are for QD-B (QD-C).

stresses in the membrane (see values of ϕ' in Table I for QD-B and in Table II for QD-C) do not coincide with that of the QD's elongation direction, i.e., the [110] direction for our QDs.

The anticrossing of the X^0 states is usually accompanied by sigmoidal change in the polarization directions of the two emission lines. These changes typically look symmetric around the FSS lower bound and preserve the orthogonality between the states (i.e., $\Delta\phi = 90°$) [7–9,23,30]; see, e.g., Figs. 3(c)–3(e) of Ref. [7]. The F_p-dependent polarization directions for QD-B and QD-C, shown in Figs. 4(b) and 4(f), respectively, neither show sigmoidal changes nor preserve the angular distance between the states due to unequal variations of ϕ_L and ϕ_H as a function of F_p. This leads to a variation of $\Delta\phi$ in the range of $\sim 40°$ to $\sim 90°$, signifying that stress can be used to tune the angle between the X^0 states. It is worth noting that for $F_p < (>)\ F_p^*$, ϕ_L vs F_p has a larger (smaller) slope than ϕ_H vs F_p. This indicates switching of the polarization behavior between the two X^0 states as evident from Figs. 4(c) and 4(g), which show that the ratio I_H/I_L is less (greater) than 1 for $F_p < (>)\ F_p^*$; i.e., the low-energy X^0 lines are brighter at low F_p [see Fig. 4(g)] whereas the high-energy X^0 line is brighter at high F_p. We attribute the peculiar behavior of the X^0 emission upon application of stress to strong HH-LH mixing.

TABLE I. Measured parameters [polarization angle ϕ', intensity ratio $I_\perp/I_\parallel$ of low-energy emission of strained GaAs, splitting ΔE_{bulk} between low-energy E_1 and high-energy emission E_2, and E_1 and E_2 (in parentheses)] and calculated parameters (stress anisotropy c, minor stress value σ, and E_1 and E_2) used for stress estimation at the QD-B location on the membrane. The units for F_p, ϕ', ΔE_{12}, σ, and E_1 and E_2 are kV/cm, degrees, meV, MPa, and eV, respectively.

F_p	ϕ'	$I_\perp/I_\parallel$	ΔE_{bulk}	c	σ	E_1	E_2
−6.7	−49	0.090	21	2.33	198	1.4803 (1.4802)	1.5013 (1.5008)
0.0	−45	0.082	16	2.40	146	1.4888 (1.4896)	1.5048 (1.5053)
6.7	−47	0.135	12	2.00	132	1.4945 (1.4978)	1.5065 (1.5095)
13.3	−54	0.162	10	1.89	117	1.4976 (1.5037)	1.5076 (1.5134)
20.0	−63	0.209	10	1.77	125	1.4973 (1.5072)	1.5073 (1.5163)
33.3	−76	0.234	12	1.79	151	1.4936 (1.5107)	1.5056 (1.5230)

TABLE II. Same as Table I, but for QD-C.

F_p	ϕ'	$I_\perp/I_\parallel$	ΔE_{bulk}	c	σ	E_1	E_2
−6.7	−43	0.095	22	2.27	213	1.4785 (1.4783)	1.5005 (1.5007)
0.0	−37	0.084	17	2.42	155	1.4870 (1.4882)	1.5041 (1.5051)
6.7	−32	0.152	11	1.96	125	1.4959 (1.4980)	1.5070 (1.5087)
13.3	−33	0.232	9	1.67	119	1.4988 (1.5037)	1.5079 (1.5124)
20.0	−36	0.414	7	1.35	110	1.5020 (1.5081)	1.5090 (1.5153)
26.7	−51	0.454	6	1.31	96	1.5039 (1.5115)	1.5099 (1.5177)
33.3	−66	0.454	6	1.34	95	1.5039 (1.5143)	1.5098 (1.5198)

B. Stress estimation: *in situ* "strain gauge"

The free-excitonic μ-PL emission of bulk-GaAs at the QD's location was analyzed to quantify the stress inside the membrane. Above the QD layer and a 7-nm-thick $Al_{0.44}Ga_{0.56}As$ barrier there is a 99-nm-thick GaAs layer. We measure PL signal from this layer using the same illumination spot as for the corresponding QD. Figure 5(a) shows a sketch of the stress conditions in the membrane in our experiment, assuming negligible out-of-plane components of the stress tensor. $\sigma_1 = \sigma$ and $\sigma_2 = c\sigma$ are the principal stresses applied at an angle of ϕ' with respect to the [110] and $[\bar{1}10]$ directions, respectively, and c is the stress anisotropy. Anisotropic biaxial stress in GaAs lifts the degeneracy of the valence bands (VBs) at Γ into two twofold-degenerate VBs [31] and mixes the HH and LH states, resulting in a polarization anisotropy of the free-excitonic emission involving these two VBs. By neglecting mixing with the split-off band and other bands, the emission intensities of these transitions at an angle ϕ with

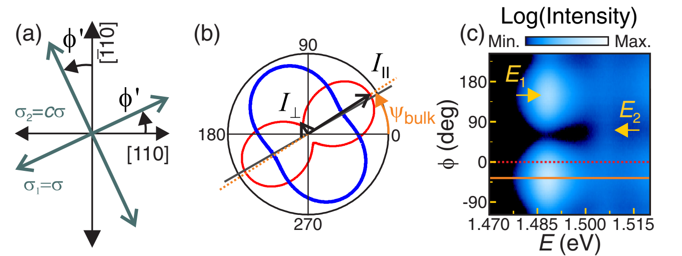

FIG. 5. (Color online) (a) Schematic representation of stress configuration in the membrane. (b) Polar plot of the calculated intensities of the low-energy (thin line) and high-energy (thick line) bulk-GaAs emission peaks at $\sigma = 1$ GPa, $c = 2$, and $\phi' = 30°$. (c) Example of μ-PL polarization map of bulk-GaAs emission from the membrane.

respect to the [110] crystal direction can be obtained by

$$I_1(\phi) \propto \left| \frac{R_\varepsilon^\dagger}{\sqrt{2}} e^{-i\phi} + \frac{Q_\varepsilon + \sqrt{Q_\varepsilon^2 + |R_\varepsilon|^2}}{\sqrt{6}} e^{i\phi} \right|^2, \quad (1)$$

$$I_2(\phi) \propto \left| \frac{R_\varepsilon^\dagger}{\sqrt{2}} e^{-i\phi} + \frac{Q_\varepsilon - \sqrt{Q_\varepsilon^2 + |R_\varepsilon|^2}}{\sqrt{6}} e^{i\phi} \right|^2 \quad (2)$$

with corresponding emission energies of

$$E_{1,2}^\sigma = E_0 + S_a(1+c)\sigma \mp \tfrac{1}{2}\big[S_b^2[(1+c)^2 + 3(1-c)^2 \sin^2 2\phi'] + S_d^2(1-c)^2 \cos^2 2\phi'\big]^{\frac{1}{2}}\sigma, \quad (3)$$

respectively, where $Q_\varepsilon = -\frac{b}{2}(s_{11} - s_{12})(1+c)\sigma$ and $R_\varepsilon^\dagger = [\frac{d}{4}s_{44}\cos 2\phi' + i\frac{\sqrt{3}}{2}b(s_{11}-s_{12})\sin 2\phi'](1-c)\sigma$ are the terms of the coordinate-transformed 4×4 Pikus-Bir Hamiltonian [32], $E_0 = E_g + E_b = 1.515$ eV, E_b is the free-excitonic binding energy in the GaAs, $S_a = a(s_{11} + 2s_{12})$, $S_b = b(s_{11} - s_{12})$, $S_d = (ds_{44})/2$, $s_{11} = 0.0114$ GPa^{-1}, $s_{12} = -0.0035$ GPa^{-1}, and $s_{44} = 0.0163$ GPa^{-1} are the elements of the elastic compliance tensor of GaAs at 10 K for the coordinate axes of the [100], [010], and [001] directions and are calculated using temperature-dependent values of elastic-tensor elements [33], and $a = a_c - a_v = -8.33$ eV, $b = -1.76$ eV, and $d = -4.55$ eV are the hydrostatic, tetragonal, and rhombohedral deformation potentials [32]. See Appendix for the transformation and for the derivation of the above equations. The polar plot in Fig. 5(b) shows the calculated normalized emission intensities for these transitions at unit stress ($\sigma = 1$ GPa), $c = 2$, and $\phi' = 30°$ using Eq. (1) (thin line) and Eq. (2) (thick line) and it shows polarization anisotropies in the emission. Figure 5(c) shows a typical polarization map for bulk-GaAs emission from the membrane at $F_p = 0$. Similarly to Fig. 5(b), it does show a strongly (weakly) polarized peak at an energy of ∼1.488 (∼1.506) eV. The polarized emission above 1.515 eV is the shoulder of the QD's ensemble emission, as these measurements were performed at relatively high excitation power.

Polarization anisotropy for strained GaAs has been reported previously [34] and is caused by finite HH-LH mixing due to nonzero off-diagonal terms in the Pikus-Bir (PB) Hamiltonian [32]. Although the emission intensities of these peaks for a given polarization angle ϕ depend on the absolute magnitude of σ, the ratios of the intensities perpendicular to the polarization direction ($I_\perp$) and along the polarization direction ($I_\parallel$) only depend on c and ϕ'. Figure 5(b) shows that the polarization direction of the polarized peaks (also referred to as phase of mixing, $\psi_{\rm bulk}$; see the dotted line) and the minor stress axis (solid line) almost coincide with each other and, for our experimental condition, the maximum angular differences between them are within the measurement error of ±2°. Therefore, the values of c can be estimated by measuring the intensity ratio and $\phi' \simeq \psi_{\rm bulk}$. Using the values of c, $\psi_{\rm bulk}$, and the measured energetic splitting ($\Delta E_{\rm bulk}$) between the free-excitonic peaks, the value of σ can be easily estimated. In order to estimate the F_p-dependent stress inside QD-B and QD-C, we performed polarization maps of the bulk-GaAs emission peaks at their locations at each F_p. The intensity ratios and $\psi_{\rm bulk}$ of the low-energy free-excitonic peak were used to estimate the values of c. Tables I and II summarize the values of measured ϕ', intensity ratio $I_\perp/I_\parallel$, and $\Delta E_{\rm bulk}$ and calculated c and σ for both QDs. The changes in ϕ' with F_p indicate that the applied biaxial stress is anisotropic and its principal axes do not coincide with those of the pre-stress induced by the bonding process. The origin of stress anisotropy is not yet understood. In addition, we note that the absolute peak emission energies of both strain-split GaAs transitions (see last two columns of both tables), calculated using Eq. (3), deviate from the measured ones (values within parentheses). The presence of out-of-plane stress components due to undesirable local bending of the membranes may account for the discrepancies and will be a subject of further investigation. For identifying possible sources of the observed pre-stress in the membranes, we consider here the effect of sample cooling after the gold-thermocompression bonding process, as discussed in the next section.

C. Thermal stress

Unequal thermal contractions of the different materials can produce thermal stress. To quantify this effect, we measured the temperature dependence of the free-excitonic emission energies of bulk GaAs from the as-grown sample [see Fig. 6(a)] and from a gold-bonded membrane [see Fig. 6(b)]. Figure 6(a) shows that the temperature dependence of the measured (closed circles) energies of bulk GaAs from the as-grown sample nicely follow the Varshni's relation (solid line) of the temperature dependence of the band gaps of GaAs. This is expected since all the layers of the as-grown sample are almost lattice matched and have also nearly equal thermal expansion coefficients (5.73×10^{-6} °C^{-1} after Ref. [35]), so that the strain

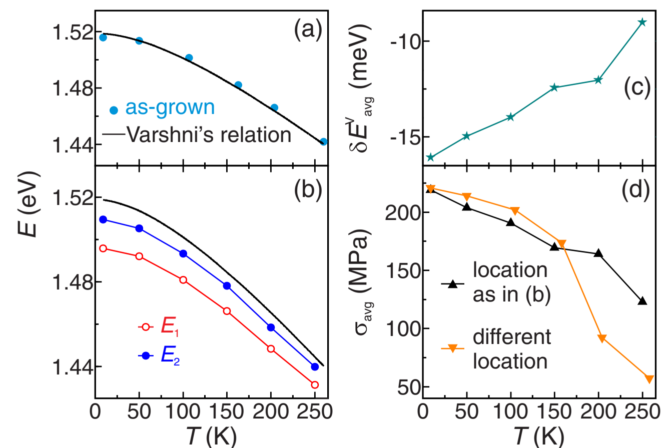

FIG. 6. (Color online) (a) Temperature- (T-) dependent free-excitonic emission energies (closed circles) of bulk GaAs from the as-grown sample. (b) T-dependent measured peak emission energies for low- (open circles) and high- (closed circles) energy transitions, i.e., E_1 and E_2, respectively, of bulk GaAs from a gold-bonded membrane. The solid lines in (a) and (b) represent the Varshni's relation for the T dependence of GaAs band gaps. (c) Energetic deviations of the average emission energies of the doublet from the band gaps of GaAs given by Varshni's relation, i.e., $\delta E_{\rm avg}^{\rm V} = E_{\rm avg} - E_{\rm Varshni}$, as a function of T at the location as in (b). (d) T-dependent estimated average of principal stresses at the location as in (b) and (c) (up-triangles) and at a different location on the same membrane (down-triangles).

developed in the layer of GaAs will be negligible. Thus, we can use the values of band gap energies obtained from the Varshni's relation as a reference to estimate the thermal stress in the membranes.

As can be seen from Fig. 6(b), the free-excitonic emission energies of the low- (open circles) and high- (closed circles) energy transitions of bulk GaAs from the membrane at all temperatures are lower than the energies given by Varshni's relation. This indicates that the membrane is under tensile stress at all temperatures. As T decreases, the energetic deviation of the average emission energy of the GaAs doublet [$E_{\text{avg}} = (E_1 + E_2)/2$] from the band gap of GaAs given by Varshni's relation, i.e., $\delta E^{\text{V}}_{\text{avg}} = E_{\text{avg}} - E_{\text{Varshni}}$ [see Fig. 6(c)] increases. The increased redshifts of the GaAs emission doublet suggest that the cooling process imposes an additional stress in the membrane. We estimated the stresses in the membrane at each T, using the measured emission energies of bulk GaAs in Eq. (A14) at $F_{\text{p}} = 0$ and by replacing E_0 with T-dependent band gap energies $E_{\text{Varshni}}(T)$. We calculate the average of the principal stresses at each temperatures at two different locations on the same membrane using the following relation derived from Eq. (A15):

$$\sigma_{\text{avg}}(T) = \frac{1}{2S_a}[E_{\text{avg}}(T) - E_{\text{Varshni}}(T)], \quad (4)$$

which are plotted in Fig. 6(d). At 10 K, we measure similar values of about 220 MPa thermal-stress at both locations. These values are comparable to the values of pre-stresses we measured at QD-B (∼248 MPa) and QD-C (∼265 MPa) locations, which indicates that thermal stress is one of the main factors contributing to the pre-stress at low temperatures. In addition, we see that close to room temperatures ∼50–125 MPa thermal stress is present into the membrane. We ascribe this to the bonding process, which was performed at a temperature of about 600 K.

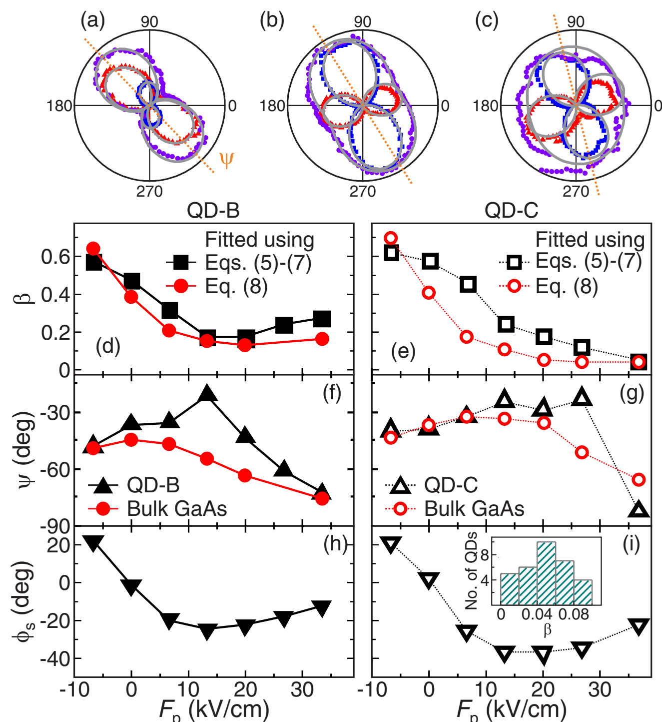

FIG. 7. (Color online) Polar plots of the intensities of the low-energy (triangles), high-energy (squares), and total intensities (circles) of X^0 lines at $F_{\text{p}} = -6.7$ (a) and 26.7 kV/cm (b) for QD-B and 36.7 kV/cm (c) for QD-C. The solid lines are the fits using Eqs. (1)–(3). Plots of (d) β, (f) ψ, and (h) ϕ_{s} versus F_{p} for QD-B. (e), (g), and (i) Similar plots for QD-C. Circles are the fitted values using the measured stresses and Eq. (8) and all other symbols are estimated using fits of the QD's X^0 emission intensities using Eqs. (5)–(7). Inset of (i): Histograms of β for as-grown QDs.

D. HH-LH mixing and HH-LH splitting in QDs

For GaAs QDs, in which the elongation axis usually aligns with the [110] direction, the low- and high-energy lines can be represented by the states $|L\rangle = (|+1^{\text{m}}\rangle - |-1^{\text{m}}\rangle)/\sqrt{2}$ and $|H\rangle = -i(|+1^{\text{m}}\rangle + |-1^{\text{m}}\rangle)/\sqrt{2}$, respectively, where $|\pm 1^{\text{m}}\rangle = \sqrt{1-\beta^2}e^{\pm i\phi_{\text{s}}}|\pm 1^{\text{hh}}\rangle - \beta e^{\pm i(2\psi+\phi_{\text{s}})}|\mp 1^{\text{lh}}\rangle$ are the HH-LH mixed bright X^0 states, $|\mp 1^{\text{hh(lh)}}\rangle$ are the X^0 states with $\mp\hbar$ projections of the total angular momentum of heavy- (light-) hole neutral exciton on the quantization axis, β is the amplitude of mixing, ψ is the phase of mixing which represents the polarization direction of the partially linearly polarized total intensities of both X^0 lines [see dotted lines in Figs. 7(a)–7(c)], and ϕ_{s} is the QD symmetry axis. We fit simultaneously the measured intensities of low- and high-energy X^0 lines, and their sum with their respective emission intensity equations:

$$I_{\text{X}}(\phi) = N[\beta' \cos(\phi + \phi_{\text{s}}) + r\beta \cos(\phi - \phi_{\text{s}} - 2\psi)]^2, \quad (5)$$

$$I_{\text{Y}}(\phi) = N[\beta' \sin(\phi + \phi_{\text{s}}) - r\beta \sin(\phi - \phi_{\text{s}} - 2\psi)]^2, \quad (6)$$

$$I_{\text{T}}(\phi) = I_{\text{X}} + I_{\text{Y}} = N[\beta'^2 + r^2\beta^2 + 2r\beta'\beta \cos 2(\phi - \psi)], \quad (7)$$

where the proportionality constant $N = |\langle\chi^{\text{e}}|\chi^{\text{hh}}\rangle|^2/3$, $\langle\chi^{\text{e}}|\chi^{\text{hh}}\rangle$ is the electron–heavy hole (e-hh) overlap integral, $r = |\langle\chi^{\text{e}}|\chi^{\text{lh}}\rangle|/|\langle\chi^{\text{e}}|\chi^{\text{hh}}\rangle|$ is the overlap ratio, and $\beta' = \sqrt{3(1-\beta^2)}$. The fitting parameters are N, r, β, ψ, and ϕ_{s}. To avoid mutual dependency between the fitting parameters β and r, $r = 1$ was assumed (see below further discussion about this assumption). Assuming no out-of-plane stress in our QDs, the out-of-plane HH-LH mixing, which influences the in-plane intensities little (see Ref. [13]), has not been considered for the derivation of the above equations. Examples of the fitting results for QD-B and for QD-C are shown in Figs. 7(a)–7(c). The mixing parameters extracted from the fits for different values of F_{p} are also summarized in Fig. 7. The β, which takes into account all the possible factors that affect the symmetry of the hole wave function, e.g., QD shape elongation, stress, and Coulomb interactions [36], can be tuned in the range of ∼8% to ∼70%, as shown in Fig. 7(d) for QD-B and in 7(e) for QD-C.

As our as-grown QDs show an average value of β of only 0.05, as shown by the histogram in the inset of Fig. 7(i), the combined effects of shape anisotropy and Coulomb interaction do not appear to lead to a large polarization anisotropy for our QDs. Therefore, the measured β are mainly due to the applied stresses and thus can be approximated by

$$\beta \approx \frac{2|R_\varepsilon|}{\sqrt{2(\Delta E_{\text{qc}} - \Delta E_{\text{bulk}})(2Q_\varepsilon + \Delta E_{\text{qc}} - \Delta E_{\text{bulk}})}}, \quad (8)$$

where ΔE_{qc} and ΔE_{bulk} are the HH-LH splitting in the as-grown QDs due to quantum confinement and in the bulk GaAs due to stress, respectively. We fit β [squares in Figs. 7(d) and 7(e)] using Eq. (8) and with only ΔE_{qc} as a fitting parameter. The fitted β [circles in Figs. 7(d) and 7(e)] are in good agreement with β extracted from the intensity fits. The reason for the discrepancy (specially for QD-C) could be due to the assumption $r = 1$ in the intensity fits. As shown in Fig. 4(d) for QD-B and in Fig. 4(h) for QD-C, the measured maximum total intensity, which also represents N for Eqs. (5)–(7), changes by a factor of $\sim$2 in the complete tuning range. This indicates that stress in the QDs does influence the e-hh overlap integral. Since LHs have a different symmetry compared to HHs the e-lh overlap integral may vary from the e-hh overlap integral, causing a variation of r. Hence, the intensity fits may not give proper values of β. The values of ΔE_{qc} obtained from the fits are 28.0 ± 5.6 meV for QD-B and 28.4 ± 11.4 meV for QD-C. These values are reasonable because the investigated QDs, with lateral dimensions in the range of 40–60 nm, are relatively large, so that the quantization energies of holes will be mainly governed by the dot height, which is in the range of 8–10 nm. Using a quantum-well model this corresponds to ΔE_{qc} of 45–29 meV. The maximum value of ΔE_{bulk} measured is 22 meV, and under the tensile stress condition the ΔE_{qc} will be reduced by the same amount. This indicates that a slightly larger tensile stress would be sufficient to switch over the character of the ground state of holes from the usual HH to LH, which has recently been realized by Huo *et al.* [26] by embedding similar QDs into MBE-grown pre-stressed membranes.

It should be noted that tuning of HH-LH mixing and measurement of stress allows us to estimate the HH-LH splitting (an intrinsic parameter) of QDs. Similar measurements can also be transferred to widely used InGaAs QDs for tuning the HH-LH mixing over a broad range. This could be achieved, for example, by integrating them into a MBE-grown pre-stressed membrane [26,37]. If layers of the membrane are properly engineered then they could provide an additional tensile stress to the QDs, which would bring HH and LH states closer to each other, thus enhancing the HH-LH coupling.

E. Stress-dependent QD symmetry axis

Figures 7(f) and 7(g) present comparisons of ψ for QDs (triangles) with ψ_{bulk} for bulk GaAs (circles). In the low-F_{p} regime, where the stresses are larger (see Table I), ψ almost follows ψ_{bulk} because the stress-induced polarization anisotropy dominates over the shape-induced polarization anisotropy of QDs. Conversely, in the high-F_{p} regime, ψ for QDs are determined by shape-induced polarization anisotropy due to reduced stress. Since the stress-induced phases of mixing (i.e., the measures of stress-induced symmetry axis) do not coincide with the axis of symmetry of the as-grown QDs (close to the [110] or [$\bar{1}$10] directions), the resultant symmetry axes, i.e., ϕ_{s}, will no longer coincide with the crystallographic directions as shown in Fig. 7(h) for QD-B and in Fig. 7(i) for QD-C. Similar to FSS minima, shown in Fig. 4(a) for QD-B and in Fig. 4(e) for QD-C, the rotations of ϕ_{s} for both QDs show minima at F_{p} values close to F_{p}^*, which indicate the anticrossing of the X^0 states. However, we do not observe sigmoidal-type changes in the polarization directions of the X^0 states [see Figs. 4(b) and 4(f)]. Therefore, the presented investigations can be described as anomalous anticrossing behavior of X^0 states in the large HH-LH mixing regime.

IV. CONCLUSION

In summary, we have shown that fine-structure and polarization properties of the X^0 states of the QDs in the large HH-LH mixing regime can be substantially different from the usually observed properties in the case of small or no mixing. Large mixing is induced by applying anisotropic stress to initially unstrained GaAs QDs with high optical quality. Stress is varied by placing semiconductor membranes with embedded QDs on top of piezoelectric actuators and it is quantified by polarization-resolved photoluminescence of the membrane material. Stress-induced mixing leads to fine-structure split X^0 lines with nonorthogonal polarizations, so that such lines cannot be described by the usual horizontal $|H\rangle$ and vertical $|V\rangle$ notations on the Poincaré sphere. The stress-dependent variations of FSS and polarization directions of neutral exciton states do not show the usually observed sigmoidal-type variation in polarization directions and orthogonality between these two states. In addition, we have also shown that the tuning allows us to estimate HH-LH splitting, which is an intrinsic parameter of the dots. The broadband tuning of HH-LH mixing could also be achieved for widely used InGaAs QDs by engineering the stress condition of the membrane into which they are embedded. The on-chip tuning technique presented here shows therefore an exciting possibility for the investigation of spin dynamics of a hole as a function of HH-LH mixing.

ACKNOWLEDGMENTS

We acknowledge Y. H. Huo, K. F. Liao (NCTU), B. Höfer, J. X. Zhang, and S. Böttner for fruitful discussions and B. Eichler, R. Engelhard, and J. R. Schröter for technical support. This work was supported by the DFG (FOR730), BMBF (QuaHL-Rep, Contract No. 01BQ1032), EU HANAS (Contract No. 601126), EPSRC, and the Royal Society.

APPENDIX

Since we are interested in optical measurements involving the lowest direct band gap region, e.g., at Γ in GaAs, we will restrict ourselves to the effect of strain on the bands at Γ. Therefore, the conduction-band (CB) energy at the Γ point will be given by

$$E_{\mathrm{c}}(\varepsilon_{ij}) = E_{\mathrm{g}} + a_{\mathrm{c}}(\varepsilon_{xx} + \varepsilon_{yy} + \varepsilon_{zz}), \qquad \text{(A1)}$$

where E_{g} is the band gap of GaAs and the extremum of the degenerate HH and LH valence bands (VBs) of unstrained GaAs is set at zero energy, a_{c} is the hydrostatic deformation potential for the CBs, $i,j \in \{x,y,z\}$, x,y, and z represent the [110], [$\bar{1}$10], and [001] crystal directions, respectively, and ε_{ij} represent the components of the strain tensor. If we exclude the coupling to split-off bands then the Hamiltonian of the VBs for strained GaAs at Γ [the so-called Pikus-Bir (PB) Hamiltonian]

in the basis of $(|\frac{3}{2},\frac{3}{2}\rangle,|\frac{3}{2},\frac{1}{2}\rangle,|\frac{3}{2},-\frac{1}{2}\rangle,|\frac{3}{2},-\frac{3}{2}\rangle)$ is written as

$$H_{\varepsilon}^{\mathrm{PB}}=-\begin{bmatrix} P_{\varepsilon}+Q_{\varepsilon} & -S_{\varepsilon} & R_{\varepsilon} & 0 \\ -S_{\varepsilon}^{\dagger} & P_{\varepsilon}-Q_{\varepsilon} & 0 & R_{\varepsilon} \\ R_{\varepsilon}^{\dagger} & 0 & P_{\varepsilon}-Q_{\varepsilon} & S_{\varepsilon} \\ 0 & R_{\varepsilon}^{\dagger} & S_{\varepsilon}^{\dagger} & P_{\varepsilon}+Q_{\varepsilon} \end{bmatrix}, \tag{A2}$$

where the basis functions are

$$\begin{aligned} \left|\frac{3}{2},\frac{3}{2}\right\rangle &= -\frac{1}{\sqrt{2}}\,|(X+iY)\uparrow\rangle\,, \\ \left|\frac{3}{2},\frac{1}{2}\right\rangle &= -\frac{1}{\sqrt{6}}\,|(X+iY)\downarrow\rangle+\sqrt{\frac{2}{3}}\,|Z\uparrow\rangle\,, \\ \left|\frac{3}{2},-\frac{1}{2}\right\rangle &= \frac{1}{\sqrt{6}}\,|(X-iY)\uparrow\rangle+\sqrt{\frac{2}{3}}\,|Z\downarrow\rangle\,, \\ \left|\frac{3}{2},-\frac{3}{2}\right\rangle &= \frac{1}{\sqrt{2}}\,|(X-iY)\downarrow\rangle\,, \end{aligned} \tag{A3}$$

where $\mp\frac{1}{\sqrt{2}}\,|X\pm iY\rangle$ and $|Z\rangle$ are the $Y_{1\pm 1}$ and Y_{10} spherical harmonics, respectively, and

$$P_{\varepsilon}=-a_{\mathrm{v}}(\varepsilon_{xx}+\varepsilon_{yy}+\varepsilon_{zz}), \tag{A4}$$

$$Q_{\varepsilon}=-\frac{b}{2}(\varepsilon_{xx}+\varepsilon_{yy}-2\varepsilon_{zz}), \tag{A5}$$

$$R_{\varepsilon}=\frac{d}{2}(\varepsilon_{xx}-\varepsilon_{yy})-i\sqrt{3}b\varepsilon_{xy}, \tag{A6}$$

$$S_{\varepsilon}=-d(\varepsilon_{xz}-i\varepsilon_{yz}). \tag{A7}$$

Under the condition of no out-of-plane shear strains inside the crystal, the energies of the top two twofold-degenerate VBs at Γ ($\mathbf{k}=0$) will be given by

$$E_{\mathrm{v1,v2}}=-P_{\varepsilon}\pm\sqrt{Q_{\varepsilon}^{2}+|R_{\varepsilon}|^{2}}, \tag{A8}$$

where the subscripts "v1" and "v2" represent the top two VBs. The above equations can be easily obtained by diagonalizing the transformed PB Hamiltonian represented by Eq. (A2). Thus, the absolute energetic splitting between these two VBs can be defined as

$$\Delta E_{\mathrm{bulk}}=2\sqrt{Q_{\varepsilon}^{2}+|R_{\varepsilon}|^{2}}. \tag{A9}$$

For the stress condition, as described schematically in Fig. 5(a) and using the transformation matrix $\mathrm{T}_z(\phi')$ (see Refs. [38,39]) the stress components σ_{xx} along the [110], σ_{yy} along the $[\bar{1}10]$ crystal direction, and shear stress σ_{xy} will be given by

$$\begin{bmatrix}\sigma_{xx}\\ \sigma_{yy}\\ \sigma_{xy}\end{bmatrix}=\begin{bmatrix}\cos^{2}\phi' & \sin^{2}\phi' & -\sin 2\phi' \\ \sin^{2}\phi' & \cos^{2}\phi' & \sin 2\phi' \\ \frac{1}{2}\sin 2\phi' & -\frac{1}{2}\sin 2\phi' & \cos 2\phi'\end{bmatrix}\begin{bmatrix}\sigma\\ c\sigma\\ 0\end{bmatrix}. \tag{A10}$$

Using the inverse Hook's law,

$$\begin{bmatrix}\varepsilon_{xx}\\ \varepsilon_{yy}\\ \varepsilon_{zz}\\ 2\varepsilon_{xy}\end{bmatrix}=\begin{bmatrix}s'_{11} & s'_{12} & s'_{13} & 0\\ s'_{21} & s'_{22} & s'_{23} & 0\\ s'_{31} & s'_{32} & s'_{33} & 0\\ 0 & 0 & 0 & s'_{66}\end{bmatrix}\begin{bmatrix}\sigma_{xx}\\ \sigma_{yy}\\ \sigma_{zz}\\ \sigma_{xy}\end{bmatrix}, \tag{A11}$$

where the 4×4 matrix on right-hand side of Eq. (A11) represents the transformed elastic compliance tensor of the cubic crystal for the coordinate axes of the [110], $[\bar{1}10]$, and [001] directions and are related to the elastic compliance tensor for the coordinate axes of the [100], [010], and [001] directions as follows,

$$\begin{aligned} s'_{11} &= s'_{22}=\tfrac{1}{2}(s_{11}+s_{12})+\tfrac{1}{4}(s_{44}), \\ s'_{12} &= s'_{21}=\tfrac{1}{2}(s_{11}+s_{12})-\tfrac{1}{4}(s_{44}), \\ s'_{13} &= s'_{23}=s'_{31}=s'_{32}=s_{12}, \\ s'_{33} &= s_{11}, \\ s'_{66} &= 2(s_{11}-s_{12}), \end{aligned} \tag{A12}$$

the strain components in terms of stresses can be obtained and, hence, the volumetric strain $\delta V/V$ and the terms of the PB Hamiltonian will be given by

$$\begin{aligned} \frac{\delta V}{V} &= (\varepsilon_{xx}+\varepsilon_{yy}+\varepsilon_{zz})=(s_{11}+2s_{12})(1+c)\sigma, \\ P_{\varepsilon} &= -a_{\mathrm{v}}(s_{11}+2s_{12})(1+c)\sigma, \\ Q_{\varepsilon} &= -\frac{b}{2}(s_{11}-s_{12})(1+c)\sigma, \\ R_{\varepsilon} &= \left[\frac{d}{4}s_{44}\cos 2\phi'-i\frac{\sqrt{3}}{2}b(s_{11}-s_{12})\sin 2\phi'\right](1-c)\sigma. \end{aligned} \tag{A13}$$

The stress-dependent transition energies of free-excitonic doublet at Γ will be given by

$$\begin{aligned} E_{1,2}^{\sigma} &= E_{0}+S_{a}(1+c)\sigma \\ &\mp\tfrac{1}{2}\big[S_{b}^{2}[(1+c)^{2}+3(1-c)^{2}\sin^{2}2\phi'] \\ &+S_{d}^{2}(1-c)^{2}\cos^{2}2\phi'\big]^{\frac{1}{2}}\sigma, \end{aligned} \tag{A14}$$

where $E_0=E_{\mathrm{g}}+E_{\mathrm{b}}=1.515$ eV, E_{b} is the free-excitonic binding energy in the GaAs, $S_a=a(s_{11}+2s_{12})$, $S_b=b(s_{11}-s_{12})$, $S_d=(ds_{44})/2$, and $a=a_{\mathrm{c}}-a_{\mathrm{v}}$ stands for the hydrostatic deformation potential of the zinc-blende type crystal. Thus, the average emission energy of the strain-split GaAs doublet will be given by

$$E_{\mathrm{avg}}=E_{0}+S_{a}(1+c)\sigma. \tag{A15}$$

The sign of c and the types of stress (compressive or tensile) determine which of the transitions will have a lower or higher energy. Under the conditions of tensile stress (we follow the sign convention of stress/strain, such that a positive/negative value of σ represents the case of tensile/compressive stress)

and $c \geqslant 0$, the transition indexed by 1 (2) will have a lower (higher) energy.

Using Fermi's golden rule, the emission intensities of these transitions at an angle ϕ with respect to the [110] crystal direction will be given by

$$I_1(\phi) \propto \left| \frac{R_\varepsilon^\dagger}{\sqrt{2}} e^{-i\phi} + \frac{Q_\varepsilon + \sqrt{Q_\varepsilon^2 + |R_\varepsilon|^2}}{\sqrt{6}} e^{i\phi} \right|^2,$$

$$I_2(\phi) \propto \left| \frac{R_\varepsilon^\dagger}{\sqrt{2}} e^{-i\phi} + \frac{Q_\varepsilon - \sqrt{Q_\varepsilon^2 + |R_\varepsilon|^2}}{\sqrt{6}} e^{i\phi} \right|^2.$$

The strain-induced mixing amplitude of bulk-GaAs β_{bulk} for the low-energy transition will be given by

$$\frac{\beta_{\text{bulk}}}{\sqrt{1-\beta_{\text{bulk}}^2}} = \frac{|R_\varepsilon|}{Q_\varepsilon + \sqrt{Q_\varepsilon^2 + |R_\varepsilon|^2}}. \quad \text{(A16)}$$

Using Eq. (A9), the above equation can be written as

$$\beta_{\text{bulk}} = \frac{2|R_\varepsilon|}{\sqrt{2\Delta E_{\text{bulk}}\,(2Q_\varepsilon + \Delta E_{\text{bulk}})}}. \quad \text{(A17)}$$

The quantum-confinement in the QDs splits the VBs at Γ, and the application of tensile (compressive) stress will further decrease (increase) the confinement-induced HH-LH splitting. Thus, the HH-LH mixing amplitude for stressed QDs (β) can be approximated by using Eq. (A17) by replacing ΔE_{bulk} with $(\Delta E_{\text{qc}} \mp \Delta E_{\text{bulk}})$ and Q_ε with $\pm Q_\varepsilon$ (because of the sign convention of the stress) as follows:

$$\beta \approx \frac{2|R_\varepsilon|}{\sqrt{2(\Delta E_{\text{qc}} \mp \Delta E_{\text{bulk}})(\pm 2Q_\varepsilon + \Delta E_{\text{qc}} \mp \Delta E_{\text{bulk}})}}. \quad \text{(A18)}$$

[1] D. Gammon, E. S. Snow, B. V. Shanabrook, D. S. Katzer, and D. Park, Phys. Rev. Lett. **76**, 3005 (1996).

[2] M. Bayer, G. Ortner, O. Stern, A. Kuther, A. A. Gorbunov, A. Forchel, P. Hawrylak, S. Fafard, K. Hinzer, T. L. Reinecke *et al.*, Phys. Rev. B **65**, 195315 (2002).

[3] R. J. Young, R. M. Stevenson, A. J. Shields, P. Atkinson, K. Cooper, D. A. Ritchie, K. M. Groom, A. I. Tartakovskii, and M. S. Skolnick, Phys. Rev. B **72**, 113305 (2005).

[4] G. Juska, V. Dimastrodonato, L. O. Mereni, A. Gocalinska, and E. Pelucchi, Nat. Photonics **7**, 527 (2013).

[5] T. Kuroda, T. Mano, N. Ha, H. Nakajima, H. Kumano, B. Urbaszek, M. Jo, M. Abbarchi, Y. Sakuma, K. Sakoda *et al.*, Phys. Rev. B **88**, 041306 (2013).

[6] R. M. Stevenson, R. J. Young, P. Atkinson, K. Cooper, D. A. Ritchie, and A. J. Shields, Nature (London) **439**, 179 (2006).

[7] A. J. Bennett, M. A. Pooley, R. M. Stevenson, M. B. Ward, R. B. Patel, A. Boyer de la Giroday, N. Sköld, I. Farrer, C. A. Nicoll, D. A. Ritchie *et al.*, Nat. Phys. **6**, 947 (2010).

[8] J. D. Plumhof, V. Krapek, F. Ding, K. D. Jöns, R. Hafenbrak, P. Klenovský, A. Herklotz, K. Dörr, P. Michler, A. Rastelli *et al.*, Phys. Rev. B **83**, 121302 (2011).

[9] R. Trotta, E. Zallo, C. Ortix, P. Atkinson, J. D. Plumhof, J. van den Brink, A. Rastelli, and O. G. Schmidt, Phys. Rev. Lett. **109**, 147401 (2012).

[10] C. H. Lin, W. T. You, H. Y. Chou, S. J. Cheng, S. D. Lin, and W. H. Chang, Phys. Rev. B **83**, 075317 (2011).

[11] J. D. Plumhof, R. Trotta, V. Krapek, E. Zallo, P. Atkinson, S. Kumar, A. Rastelli, and O. G. Schmidt, Phys. Rev. B **87**, 075311 (2013).

[12] Y. Léger, L. Besombes, L. Maingault, and H. Mariette, Phys. Rev. B **76**, 045331 (2007).

[13] C. Tonin, R. Hostein, V. Voliotis, R. Grousson, A. Lemaitre, and A. Martinez, Phys. Rev. B **85**, 155303 (2012).

[14] D. V. Bulaev and D. Loss, Phys. Rev. Lett. **95**, 076805 (2005).

[15] J. Fischer, W. A. Coish, D. V. Bulaev, and D. Loss, Phys. Rev. B **78**, 155329 (2008).

[16] H. J. Kimble, Nature (London) **453**, 1023 (2008).

[17] G. Bester, S. Nair, and A. Zunger, Phys. Rev. B **67**, 161306 (2003).

[18] C. Heyn, A. Stemmann, and W. Hansen, Appl. Phys. Lett. **95**, 173110 (2009).

[19] S. Kumar, R. Trotta, E. Zallo, J. D. Plumhof, P. Atkinson, A. Rastelli, and O. G. Schmidt, Appl. Phys. Lett. **99**, 161118 (2011).

[20] Y. H. Huo, A. Rastelli, and O. G. Schmidt, Appl. Phys. Lett. **102**, 152105 (2013).

[21] P. Atkinson, E. Zallo, and O. G. Schmidt, J. Appl. Phys. **112**, 054303 (2012).

[22] Y. H. Huo, B. J. Witek, S. Kumar, R. Singh, E. Zallo, R. Grifone, D. Kriegner, R. Trotta, N. Akopian, J. Stangl *et al.*, arXiv:1208.6554.

[23] R. Trotta, P. Atkinson, J. D. Plumhof, E. Zallo, R. O. Rezaev, S. Kumar, S. Baunack, J. R. Schroeter, A. Rastelli, and O. G. Schmidt, Adv. Mater. **24**, 2668 (2012).

[24] T. Belhadj, T. Amand, A. Kunold, C. M. Simon, T. Kuroda, M. Abbarchi, T. Mano, K. Sakoda, S. Kunz, X. Marie *et al.*, Appl. Phys. Lett. **97**, 051111 (2010).

[25] R. Magri and A. Zunger, Phys. Rev. B **62**, 10364 (2000).

[26] Y. H. Huo, B. J. Witek, S. Kumar, J. R. Cardenas, J. X. Zhang, N. Akopian, R. Singh, E. Zallo, R. Grifone, D. Kriegner *et al.*, Nat. Phys. **10**, 46 (2014).

[27] M. Bayer, O. Stern, A. Kuther, and A. Forchel, Phys. Rev. B **61**, 7273 (2000).

[28] D. Gammon, A. L. Efros, T. A. Kennedy, M. Rosen, D. S. Katzer, D. Park, S. W. Brown, V. L. Korenev, and I. A. Merkulov, Phys. Rev. Lett. **86**, 5176 (2001).

[29] M. Bayer, A. Kuther, A. Forchel, A. Gorbunov, V. B. Timofeev, F. Schäfer, J. P. Reithmaier, T. L. Reinecke, and S. N. Walck, Phys. Rev. Lett. **82**, 1748 (1999).

[30] R. Singh and G. Bester, Phys. Rev. Lett. **104**, 196803 (2010).

[31] F. H. Pollak and M. Cardona, Phys. Rev. **172**, 816 (1968).

[32] S. L. Chuang, *Physics of Photonic Devices* (Wiley, Hoboken, NJ, 2009).

[33] Y. A. Burenkov, Y. M. Burdukov, S. Y. Davidov, and S. P. Nikanorov, Sov. Phys. Solid State **15**, 1175 (1973).

[34] K. Rammohan, Y. Tang, D. H. Rich, R. S. Goldman, H. H. Wieder, and K. L. Kavanagh, Phys. Rev. B **51**, 5033 (1995).

[35] S. I. Novikova, Sov. Phys. Solid State **3**, 129 (1961).

[36] Y.-H. Liao, C.-C. Liao, C.-H. Ku, Y.-C. Chang, S.-J. Cheng, M. Jo, T. Kuroda, T. Mano, M. Abbarchi, and K. Sakoda, Phys. Rev. B **86**, 115323 (2012).

[37] D. L. Owen, D. Lackner, O. J. Pitts, S. P. Watkins, and P. M. Mooney, Semicond. Sci. Technol. **24**, 035011 (2009).

[38] J. F. Nye, *Physical Properties of Crystals* (Clarendon Press, Oxford, 1960).

[39] V. Yildirim, Int. J. Eng. Sci. **37**, 1007 (1999).